

Momentum-space and real-space Berry curvatures in Mn_3Sn

Xiaokang Li¹, Liangcai Xu¹, Huakun Zuo¹, Alaska Subedi^{2,3}, Zengwei Zhu^{1*}, Kamran Behnia^{4**}

1 Wuhan National High Magnetic Field Center, School of Physics, Huazhong University of Science and Technology, Wuhan 430074, China

2 Centre de Physique Théorique, École Polytechnique, CNRS, Université Paris-Saclay, 91128 Palaiseau, France

3 Collège de France, 11 place Marcelin Berthelot, 75005 Paris, France

4 Laboratoire de Physique Et Etude des Matériaux (UPMC-CNRS), ESPCI Paris, PSL Research University 75005 Paris, France

* zengwei.zhu@hust.edu.cn

** kamran.behnia@espci.fr

September 10, 2021

Abstract

Mn_3X ($\text{X} = \text{Sn}, \text{Ge}$) are non-collinear antiferromagnets hosting a large anomalous Hall effect (AHE). Weyl nodes in the electronic dispersions are believed to cause this AHE, but their locus in the momentum space is yet to be pinned down. We present a detailed study of the Hall conductivity tensor and magnetization in Mn_3Sn crystals and find that in the presence of a moderate magnetic field, spin texture sets the orientation of the k -space Berry curvature with no detectable in-plane anisotropy due to the Z_6 symmetry of the underlying lattice. We quantify the energy cost of domain nucleation and show that the multi-domain regime is restricted to a narrow field window. Comparing the field-dependence of AHE and magnetization, we find indirect evidence for real-space Berry curvature caused by these domain walls.

1 Introduction

The Mn_3X ($\text{X} = \text{Sn}, \text{Ge}$) family of compounds crystallizing in the DO_{19} HCP Bravais lattice are triangular antiferromagnets with a Néel temperature around 400 K [1, 2]. The recent observation of the anomalous Hall effect (AHE) in these systems [3–5] followed theoretical predictions [6, 7] of nonvanishing Berry curvature in a noncollinear yet planar antiferromagnet. The discovery was followed by the detection of anomalous Nernst [8, 9] and anomalous Righi-Leduc [9] effects, the thermoelectric and thermal counterparts of the AHE, respectively. The latter observations confirmed that the zero-field transverse anomalous currents are due to the Fermi-surface quasiparticles, as argued by Haldane [10]. Several *ab initio* calculations [8, 11] have found an anomalous Hall conductivity (AHC) matching what experiments find at low temperatures. The precise configuration of spins and the locus of the Weyl nodes in the k -space generating the Berry curvature that cause these phenomena are still subject to debate.

The Hall resistivity of Mn_3Sn has a peculiar profile (see Fig. 1). Recognizably different from the AHE signal resolved in ordinary ferromagnets like bcc iron [9, 12, 13] or cobalt [14],

it is also quite distinct from the much-studied spiral helimagnet MnSi [15, 16]. In contrast to these cases, in Mn₃Sn, ρ_{ij} presents a hysteretic jump dwarfing the slope caused by the ordinary Hall conductivity. The hysteresis has a shape unlike the sigmoid commonly seen in ferromagnets [17]. Finally, the asymmetry of this loop contrasts with the symmetric hysteresis of the quantum AHE observed in magnetic two-dimensional topological insulators [18, 19].

In this paper, we show that the peculiarity of this hysteresis loop resides in the existence of a threshold field B_0 for domain nucleation. Three distinct regimes can be identified. In regime I, below B_0 , there is a single magnetic domain with an orientation set by the sample history and not by the applied field. In regime II, above B_0 , multiple domains coexist, and, as the magnetic field increases, the domain favored by it occupies a larger portion of the sample. At sufficiently higher fields (regime III), the sample becomes single domain again, and the domain orientation is now entirely set by the magnetic field. Monitoring the electric field generated by a rotating in-plane magnetic field in regime III, we find that the finite component of the AHC tensor is set by the orientation of spins and not by the underlying lattice. This observation is backed by theoretical calculations, which find that the single-ion anisotropy is vanishingly small and the Fermi surface is not modified by rotation of spins. It also has implications for the ongoing effort to pin down the source of the Berry curvature in the reciprocal space. The magnitudes of B_0 and the jump in magnetization can be used to quantify the energy cost of erecting domain walls. Finally, we compare the field dependence of ρ_{ij}^A and magnetization and find that they start to deviate from each other in the multi-domain regime. Such an observation in other systems has been commonly attributed to a ‘topological Hall effect’ (THE) due to the accumulation of the Berry curvature in the real space [20], which can be caused by a non-trivial magnetic texture, such as a skyrmion lattice in the phase A of MnSi [15]. We tentatively suggest that when Mn₃Sn is multi-domain, domain walls generate a real-space Berry curvature and an additional contribution top of the one caused by momentum-space Berry curvature. This would imply a non-coplanar spin component for domain walls, which is yet to be observed by near-field probes.

2 Three distinct regimes in the hysteresis loop

Fig. 1 shows the hysteretic loop of $\rho_{ij}(B)$ at the room temperature in a millimetric Mn₃Sn single crystal. When the magnetic field attains a magnitude as low as 0.2 T, ρ_{ij} locks into a finite magnitude and does not show any further evolution besides the tiny slope due to the ordinary Hall effect. When the field is swept back to zero, $\rho_{ij}(B)$ remains locked to its magnitude. Only when the field, oriented along the opposite direction, attains a specific amplitude, which we call B_0 , $\rho_{ij}(B)$ begins to change steeply. Upon further increase, $\rho_{ij}(B)$ saturates to a value opposite in sign but identical in magnitude to its initial value. As seen in the figure, repeating this procedure numerous times with different sweeping rates reproduces the same curve. This is very different from the hysteretic magnetization profile seen in ferromagnets, which has a ‘sigmoid’ shape [17]. On the other hand, it is remarkably similar to the hysteretic loop of magnetization resolved in a ferromagnetic liquid crystal [21]. In the former case, the shape of the hysteretic loop is set by the displacement of domain walls and their pinning by defects. The loop is smooth, and the passage between single-domain and multidomain regimes in its two ends are symmetric [17].

The existence of a finite threshold field for domain nucleation implies that, below this

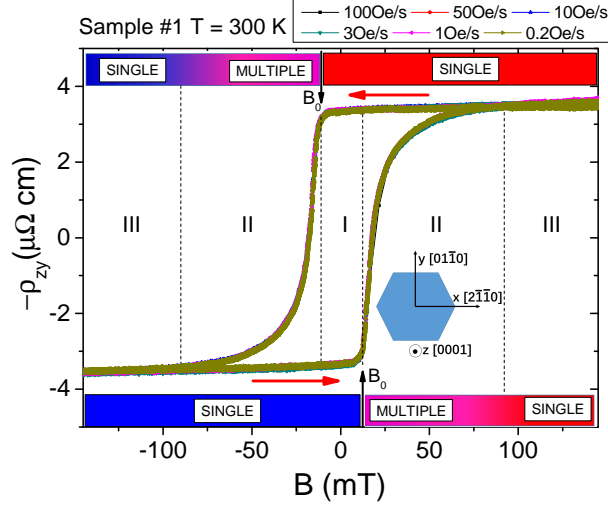


Figure 1: **Hysteretic anomalous Hall effect in Mn_3Sn :** $-\rho_{zy}^A$ as a function of magnetic field in Mn_3Sn has a peculiar shape. Three different regimes can be identified. When the field is lower than B_0 , marked by a vertical arrow, the spins keep their configuration regardless of the magnetic field (regime I). When $B > B_0$ (regime II), new magnetic domains are induced by the magnetic field. At sufficiently high fields, the sample becomes single-domain again (regime III). The hysteretic loop is reproducible even when the sweeping rate changes by a factor of five hundred.

field, tolerating a magnetization opposite to the applied field is not as costly in energy than erecting a domain wall. At B_0 , the two costs become equal and domain reversal starts. Insensitivity to the sweep rate suggests thermodynamic equilibrium during the entire loop. The boundary between regime I (single-domain) and regime II (multi-domain) is sharp, but the boundary between regime II and regime III (field-induced single domain) is fuzzy and, as we will see below, hosts a specific component in $\rho_{ij}(B)$ generated by inhomogeneous magnetization. In regime III, the signal smoothly saturates to its initial magnitude with an opposite sign, indicating an inverted single-domain regime.

3 Angle-dependent Hall conductivity

Our angle-dependent study illustrates the difference between the three regimes. In this experiment, electric current was applied along the z -axis and the magnetic field rotated in the xy plane. The electric field along different orientations was monitored using multiple electrodes. In this way, we could determine the amplitude and the orientation of the total electric-field vector for an arbitrary orientation of magnetic field. We studied both a square sample (see appendix) and a triangular sample (see Fig. 2), whose shape excluded demagnetization artifacts. The results were similar. In regime I, that is below B_0 , the electric field was unaffected by rotation. In regime II, strong hysteresis was observed in the angular dependence of the signal. In regime III, each projection of the electric field along the three x - and three y -axes was found to display almost perfect sinusoids. Thus, in this regime, the spin texture is easily

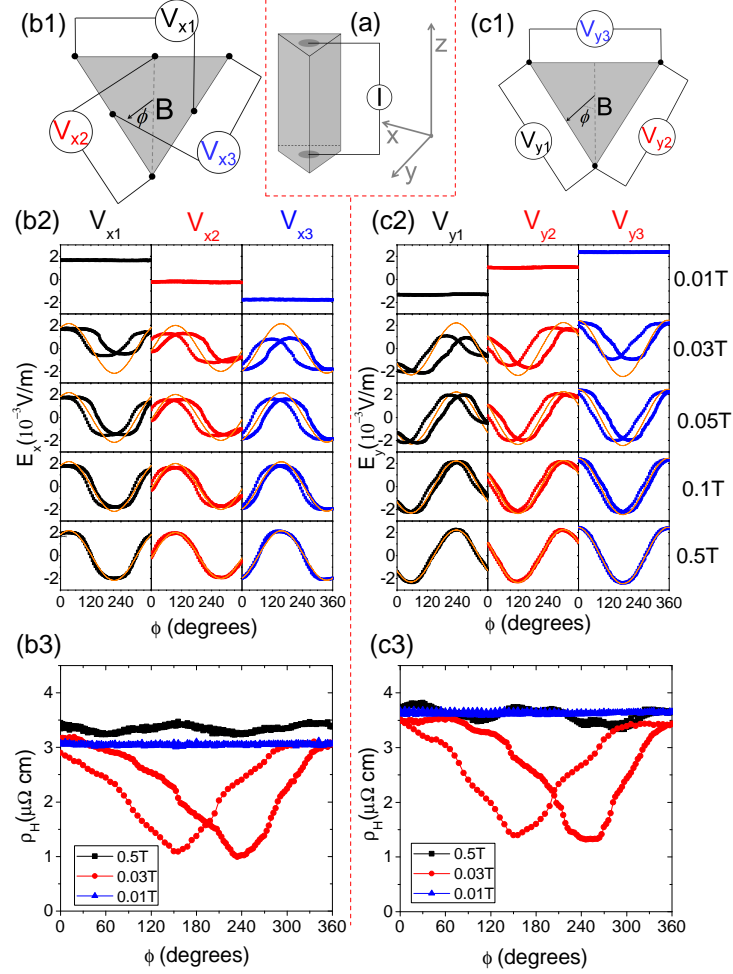


Figure 2: **Angle-dependent Hall resistivity:** a) The current was applied along the z -axis of a sample with a triangular cross section and the magnetic field was rotated in the basal plane. Each pair of electrodes monitored the electric field along one of the three equivalent x -axes (b1) or the three y -axes (c1). Angular variation of the three E_x and the three E_y as a function of the angle between magnetic field and the x -axis are shown in (b2) and (c2). At low magnetic field (regime I), the total electric field remains unchanged. At high magnetic field (regime III), the measured electric field becomes sinusoidal (shown as a red line). In the intermediate field range (regime II), the electric field is non-sinusoidal and strongly hysteretic. Panels (b3) and (c3) show $\rho_H = |E|/J$, where $|E|$ represents the magnitude of the total electric field vector extracted from its projections. It is almost the same in regimes I and III. The fluctuations in regime III set an upper bound to any in-plane anisotropy undetectable by this experiment.

rotated with magnetic field. As seen in the bottom panels of Fig. 2, in both regime I and regime III, this is when the system is single-domain, the amplitude of the electric field is the same irrespective of orientation.

4 Discussion

4.1 Single-ion anisotropy

The first outcome of this observation is that the single-ion anisotropy is very weak. A field as small as 0.5 T easily sets the orientation of the spins by coupling to the in-plane magnetization, which is $1.5 \times 10^{-2} \mu_B/\text{f.u.}$ at 0.5 T [3]. This corresponds to an energy as small as $0.5 \mu\text{eV}/\text{f.u.}$, implying a negligible single-ion anisotropy compared to the Heisenberg and Dzyaloshinskii-Moriya terms [22]. Our DFT calculations with SOC find a vanishingly small in-plane single-ion anisotropy (See appendix), with the rigid rotation of spins by a uniform angle varying the total energy by less than 0.045 meV/Mn. In agreement with previous experimental and theoretical studies [2, 3, 23], we find a noncollinear 120-degree antiferromagnetic order with a small in-plane ferromagnetic canted moment of $\sim 0.5 \times 10^{-2} \mu_B/\text{f.u.}$ Since neither the calculated total energy nor the canted component change upon a uniform rotation of the spins, the $U(1)$ symmetry is not broken to a Z_6 anisotropy.

4.2 Momentum-space Berry curvature

A second consequence is about the in-plane anisotropy of the momentum-space Berry curvature. Previous studies [3–5, 9] detected a finite AHC for two perpendicular orientations of magnetic field. The magnitude of $\sigma_{yz}^A(\mathbf{B}||x)$ and $\sigma_{xz}^A(\mathbf{B}||y)$ was found to be close to each other in both Mn_3Ge [5] and in Mn_3Sn [9]. Measuring numerous samples (See appendix), we also found that the anisotropy is small and below 15 percent (See Fig.3a). Our angle-dependent experiment puts an even smaller upper bound (~ 0.05) on any in-plane anisotropy. Our DFT calculations find a band structure (see the appendix) and a Fermi surface unchanged as the spins rotate (Fig.3b-e), in agreement with the experimental observation, which finds unchanged σ_{ij}^A for any arbitrary orientation of magnetic field in the xy plane when the current is along the z-axis and the electric field is measured perpendicular to the magnetic field.

A finite σ_{ij}^A arises when Ω^k summed over the Brillouin zone does not vanish:

$$\sigma_{ij}^A = \frac{-e^2}{\hbar} \sum_n \int_{BZ} \frac{d^3k}{(2\pi)^3} f_n(k) \Omega_n^k(k) \quad (1)$$

The indexes i , j and k refer to the three perpendicular orientations, which are often assimilated to the x -, y - and z - axes of the crystal lattice. Theoretical calculations [8, 11, 25–27] find Weyl nodes of opposite chirality in the vicinity of the k -points of the Brillouin zone of Mn_3X materials. However, they start from different magnetic structures and do not find the nodes at the same k -space position. Because of the symmetry considerations, a finite σ_{ij}^A is expected along one orientation and not the other. Our result implies that the orientation along which σ_{ij}^A remain finite is not a crystal axis. The magnitude of AHC does not depend on the angle between the spin lattice and the underlying crystal. Given the geometry of the Fermi surface in the hexagonal plane (see Fig. 3b,c), this may be accounted for by assuming that the k -space Berry curvature reside at the k -point vertices of the hexagon hosting a small

circular Fermi surface. A recent suggestion for the locus of the Weyl nodes [27] puts them close to K -points, which as one see in Fig. 3c,d host a small circular Fermi surface.

4.3 Energy cost of domain nucleation

We now turn our attention to domain nucleation at the onset of regime II. The hysteresis loop of magnetization and Hall resistivity are shown in Fig. 4a,b. A threshold field B_0 of almost identical magnitude can be identified in both. Above this field, domains with a magnetization corresponding to the orientation of the applied field nucleate in the single-domain matrix that occupies the whole sample below B_0 . As the field is swept further, the minority domain grows in size and ends up entirely replacing the former majority domain. The smooth and reproducible functional form is reminiscent of the Langevin function. However, the AHE signal increases faster than the magnetization (Fig. 4c).

The hysteresis loops were followed down to 50K, below which the magnetic order is replaced with a spin-glass order [3]. In the whole temperature window, one could detect a finite B_0 . Multiplying it by the jump in magnetization ΔM , one quantifies the energy cost per volume of keeping the sample single domain. The temperature dependence of $E_v = B_0 \Delta M$ is shown in Fig. 4d. According to the classical theory of nucleation, the first droplet of minority domains emerges when the volume energy saved by the emergence of this domain compensates the energy cost of building a domain wall E_S , which is unknown. On the other hand, the amplitude of the interaction between neighboring spins, $\langle J \rangle$, allows us to estimate a lower boundary to the thickness of the domain walls by using $t = (\frac{\langle J \rangle}{B_0 \Delta M})^{1/3}$. Given that $\langle J \rangle \sim 5\text{meV}$, which is the order of magnitude of the Heisenberg coupling between spins [22] and the size of the Néel temperature), one finds $t \geq 100\text{ nm}$ at room temperature, which is in agreement with what was suggested by Liu and Balents [22] based on the stationary solution of a sine-Gordon equation.

4.4 Real-space Berry curvature in presence of domain walls

In regime II, where the system is multi-domain, such thick domain walls can be a source of Berry curvature in real space distinct from the one provided in the momentum space by the Weyl nodes. Such a distinction between components of AHE was first demonstrated in the case of MnSi. Below its Curie temperature, this helimagnet hosts a large AHE, which is almost proportional to its magnetization across a wide temperature range [16], and is caused almost totally by momentum-space Berry curvature. In its A phase and in the presence of a skyrmion lattice, an additional component to the AHE has been resolved [15] and attributed to real-space Berry curvature, which represents an effective magnetic field caused by the spatial variation of the magnetization [20, 28, 29]. In MnSi, this specific component of the AHE caused by the momentum-space Berry curvature [15] is an order of magnitude smaller than the total anomalous signal.

Comparing the field dependence of $\rho_{ij}^A(B)$ and $M(B)$, we observe that they do not evolve identically in regime II (See Fig. 4d). One plausible interpretation is that in presence of domain walls, there is a distinct component of the AHE, which is not set by the magnitude of the global magnetization but is intimately linked to the presence of inhomogeneous magnetization caused by thick domain walls. In several other systems [30, 31], this has been attributed to a ‘topological Hall effect’ at the boundaries of a hysteresis loop. Fig. 4e shows $\rho^{THE}(B) = \rho_{ij}^A(B) - C(M(B) - B\chi)$, where χ is the high-field susceptibility (the slope of

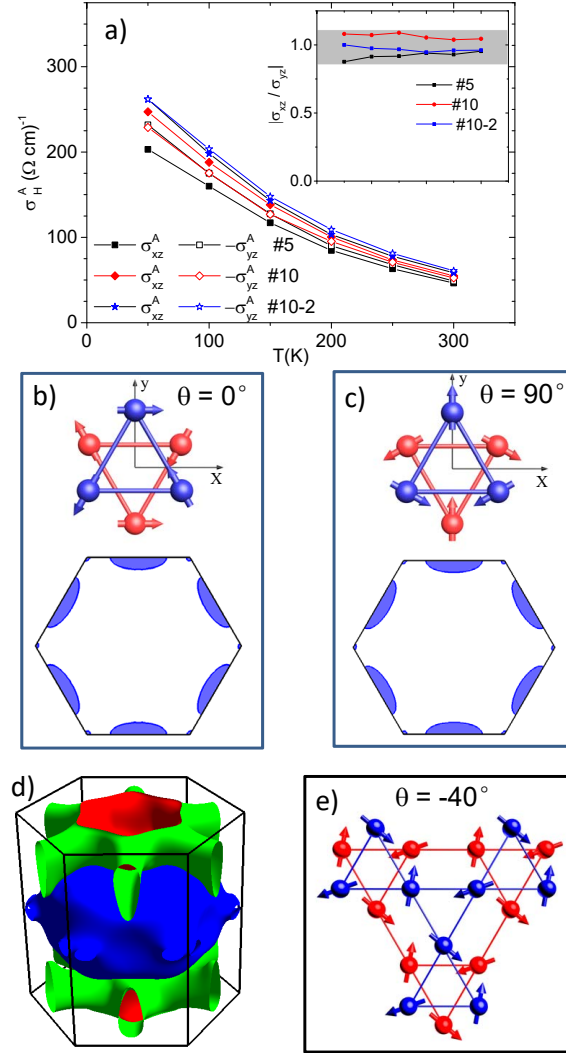


Figure 3: **In-plane isotropy:** a) Temperature-dependence of the anomalous Hall conductivity for two perpendicular orientations of the magnetic field in three different samples. The inset shows the in-plane anisotropy found in these fixed-angle measurements and the experimental margin (in gray). b,c) Mn spins in two adjacent planes (in blue and red) together with the calculated Fermi surface for each spin configuration projected in the hexagonal $(k_x, k_y, 0)$ plane of the Brillouin zone. The Fermi surface does not visibly change with spin rotation. Note also the small circular fermi surface at the vertices (the K -points). d) The calculated Fermi surface of Mn_3Sn for $\theta=0$ in three dimensions. Different colors show different Fermi surface sheets. e) Mn spins oriented along an arbitrary orientation in three adjacent six-spin David stars, each operating as a magnetic octupole [24].

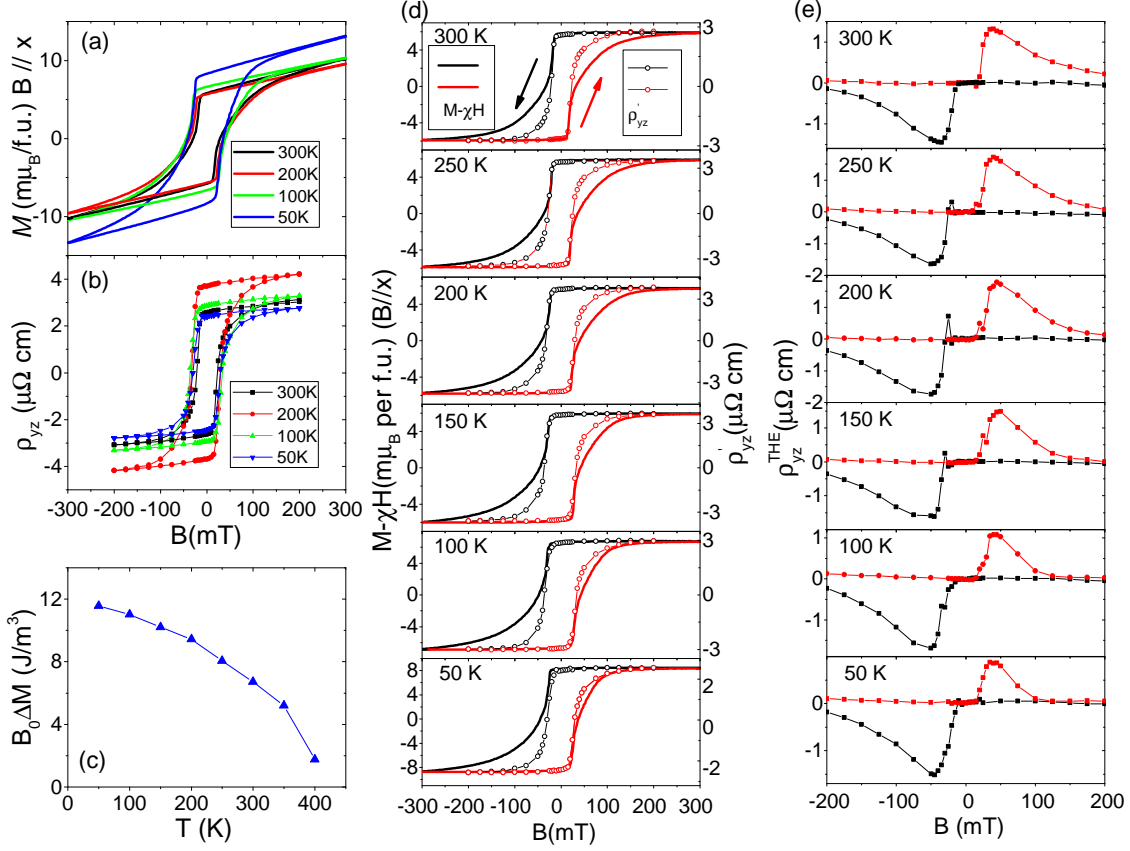


Figure 4: **Magnetization, AHE and THE:** a) Hysteretic loops of magnetization at different temperatures. b) Hysteretic loops of ρ_{yz} at different temperatures. c) Temperature dependence of $B_0\Delta M$, which represents the energy cost of staying single domain. d) Comparison of the magnetization, with its high-field slope subtracted and anomalous Hall resistivity. The threshold field B_0 is identical, but at all temperatures, the magnetization shows a slower variation towards saturation at the end of the hysteresis loop. e) ‘Topological Hall Effect’ resolved by subtracting normalized magnetization times a constant from the Hall resistivity at different temperatures. At the boundary of regimes II and III, a sizeable component of the AHE is due to inhomogeneous magnetization, with an out-of-plane component.

the magnetization outside the hysteresis loop) and C is a constant. As one can see in the figure, ρ^{THE} is finite in a narrow field window in regime II. We tentatively attribute this to the presence of thick domain walls, which introduce smoothly-changing magnetization can produce real-space Berry curvature [20].

However, a finite THE is expected to arise only if $\vec{n} \cdot (\frac{\partial \vec{n}}{\partial x} \times \frac{\partial \vec{n}}{\partial y})$ is finite [32]. Here, $\vec{n} = \vec{M}/M$ is the skyrmion density [15]. If the magnetization were restricted to the plane, $\frac{\partial \vec{n}}{\partial x} \times \frac{\partial \vec{n}}{\partial y}$ would point out of the plane and the its dot product with \vec{n} would be zero. Therefore, our interpretation implies the existence of a non-coplanar component to the magnetization of the domain walls. Such a conjecture is backed by another observation. Assuming a co-planar structure, the spin configuration of a wall between two domains of opposite orientations cannot keep the inversion symmetry preserved in each domain (See Fig. 5a). Now, a finite skyrmionic number is expected to arise in the presence of the Dzyaloshinskii-Moriya interaction and in the absence of the inversion center [33].

We note that a very recent study of Magneto-optical Kerr effect [34] confirmed that multiple domains are restricted to a narrow field window. But the internal structure of domain walls could not be resolved. Therefore, there is no direct evidence for a finite skyrmion number in the domain walls. We note however, that the component of AHE deviating from magnetization and presumably caused by the real-space Berry curvature is a sizeable fraction of the total signal. This is in sharp contrast with the case of MnSi [15]. Our interpretation implies a large skyrmion density compatible with the interatomic length scale of the change in magnetization across a domain wall in contrast to the large length scale of magnetic inhomogeneity in the skyrmion lattice of MnSi.

We found yet another manifestation of nontrivial domain walls by detecting a correlation between the width of the hysteresis loop and sample dimensions. As seen in Fig. 5b, reducing the size of a single crystal does not modify the magnitude of B_0 . On the other hand, it does affect the range of regime II in a remarkably intriguing way. The field-induced minority domain ends up eliminating the initial majority domain with a given rate B_s (See Appendix). According to the experiment, the B_s anisotropy is equal to the anisotropy of the sample dimensions parallel and perpendicular to the magnetic field (See Fig. 5c). In other words, the boundary between minority and majority domains evolves faster with increasing magnetic field along its orientation. Exploring the origin of this phenomenon and its possible connection with a bulk-edge dichotomy would be a subject matter for further theoretical and experimental studies. .

5 Conclusion

Let us summarize the picture of AHE in Mn_3X coming out of this study. Save for a narrow field window, the system remains single-domain with a spatially homogeneous magnetization. Weyl nodes in the momentum-space are believed to be responsible for the entire AHE signal in this single-domain case. There is no trace of the hexagonal symmetry of the underlying lattice in the anomalous Hall conductivity, indicating that it is entirely set by the orientation of the spin texture. We identify a narrow field window with multiple magnetic domains and therefore inhomogeneous magnetization. In this narrow window, there is a distinct contribution to the AHE which does not scale with magnetization. We suggest an interpretation for this observation by arguing that the domain walls by possessing a non-coplanar spin component

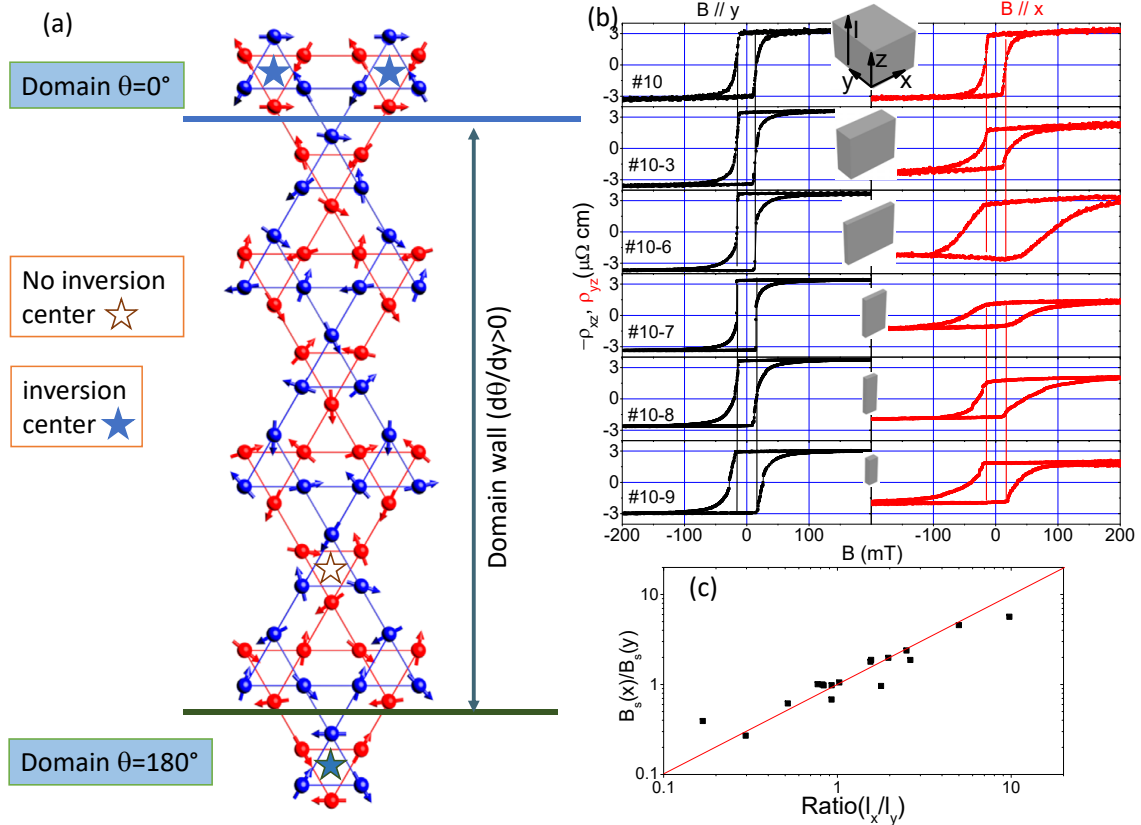


Figure 5: **Domain walls and size dependence:** a) A domain wall between two opposite domains assuming in-plane orientation for spins. Whilst in each domain, the inversion symmetry is kept, across the domain wall, it is lost due to the continuous variation of the local spin angle. This loss of inversion center provides an opportunity for the Dzyaloshinskii-Moriya interaction to generate an out-of-plane spin component, which is not shown in the present image. b) Anomalous Hall resistivity along two perpendicular orientations in a Mn_3Sn single crystal after successive reductions in the sample dimensions. Note the constancy of B_0 and the variation of the loop width. c) The anisotropy of B_s , a field scale quantifying this width (See appendix) as a function of the sample dimension ratio in a number of samples. The red solid line represents $y=x$.

could generate a real-space Berry curvature which leads to an additional component of the measured AHE on top of the one produced in the momentum space. This latter conjecture shall motivate future microscopic studies of the domain walls using high-resolution magnetic imagery techniques, such as nanomagnetometry based on single nitrogen-vacancy defect in diamond [35].

Acknowledgements

We acknowledge useful discussions with Leon Balents, Albert Fert, Jianpeng Liu, Achim Rosch, André Thiaville and Binghai Yang.

Author contributions X. L., assisted by L. X. and H. Z. performed the measurements. X. L. and Z. Z. analyzed the data. Z. Z. managed the project. A. S. carried out the calculations. K. B. wrote the paper. All authors contributed to the discussion.

Funding information Z. Z. was supported by the 1000 Youth Talents Plan and the work was supported by the National Science Foundation of China (Grant No. 11574097) and The National Key Research and Development Program of China (Grant No. 2016YFA0401704). K. B. was supported by China High-end foreign expert programme and Fonds-ESPCI-Paris. Computational resources were supported by the European Research Council grant ERC-319286 QMAC and the Swiss National Supercomputing Center (CSCS) under project s575.

A The growth and characterization of samples

Mn_3Sn single crystals were grown by the vertical Bridgman technique. For the polycrystalline samples growth, the raw materials (99.999% Mn, 99.999% Sn) were weighed and mixed inside an Ar globe box with the molar ratio of 3.3:1, and then it was put in an alumina crucible which was sealed in a quartz ampule. The growth temperature was controlled at the bottom of the ampule. The material was heated up to 1100°C, remained there for 2 hour to ensure homogeneity of the melt, and was cooled down slowly to 900°C. The sample was annealed at 850°C for 20 hours and then quenched to room temperature. For the single crystal samples growth, the polycrystalline ingot was ground and put in an alumina crucible which was sealed in a quartz tube, then was hung in a vertical Bridgman furnace. In order to get better single crystal, the single crystal sample growth was repeated three times with different rates of growth. The first growth rate is 2mm/h and the last two growth rate is 1 mm/h. The growth temperature is 1050°C and the growth length is 80mm. Both the poly-crystalline and single-crystalline samples were pulverized to powder for XRD measurement which confirmed the structure of Mn_3Sn . The single crystals were then cut into desired dimensions by a wire saw. The dimensions of some measured samples have been listed in the following tables.

B Computational details

Electronic structure calculations were performed within the generalized gradient approximation (GGA) of Perdew, Burke and Ernzerhof [36] using the general full-potential linearized augmented planewave method as implemented in the ELK software package [37]. Muffin-tin radii of 2.4 and 2.6 a.u. were used for Mn and Ir, respectively. The spin-orbit coupling was treated using a second-variational scheme. A $14 \times 14 \times 14$ k -point grid was used to perform the Brillouin zone integration, and the planewave cutoff was set by $RK_{\max} = 8$, where K_{\max} is the planewave cutoff and R is the smallest muffin-tin radius used in the calculations (i.e. 2.4 a.u.). The energy convergence criterion was set to 0.045 meV/Mn. Experimental lattice parameters $a = 5.665$ and $c = 4.531$ Å and the Mn positional parameter $x = 0.8388$ were used in all our calculations [38, 39].

C The temperature-dependence of magnetization and Hall resistivity

We measured the temperature-dependence of magnetization and Hall resistivity using a Quantum Design PPMS and VSM. In the main text, we just showed the magnetization data as the field is along x axis for a selected set of temperatures. Fig. S6 shows the complete set of data along both x and y axes at different temperatures. In all cases, we can extract the “Topological Hall Effect” (THE) also for a field along y -axis in the Fig. S7. The results for the two orientations are similar. We also measured the magnetization for a field along z at 300 K, shown in Fig. S8. Our data are similar to the previous report [3]. Fig. S8 shows the Hall resistivity and magnetization for three axis at 300 K, in which the magnetization data are similar to ref. S5.

D Measuring angle-dependence of Hall resistivity in a sample with a square cross-section

We also measured the angle-dependent Hall resistivity in a sample with a square cross section in addition to the sample with a triangular cross-section discussed in the main text. As shown in Fig. S9, two pairs of electrodes perpendicular to each other monitored the electric field along the x (E_x) and y axes (E_y). The magnetic field was rotated in the basal plane while the current was applied along its z axis. The total Hall resistance can be deduced from the two electric fields: $\rho_H = \sqrt{E_x^2 + E_y^2}/J_z$. The results were similar to the case of a sample with a triangle cross section. The three regimes can be clearly distinguished. In regime I, with a field lower than B_0 , the rotation of the magnetic field does not affect the electric field: the sample remains single domain. In regime II, sweeping the angle in the basal plane back and forth produces a strong hysteresis of the Hall resistivity. In regime III, both E_x and E_y show sinusoidal variation and no hysteresis, indicating the spin texture of the system can be rotated easily as the magnetic field. The slight variation detected in ρ_H puts an upper limit on a possible in-plane anisotropy of ρ_H .

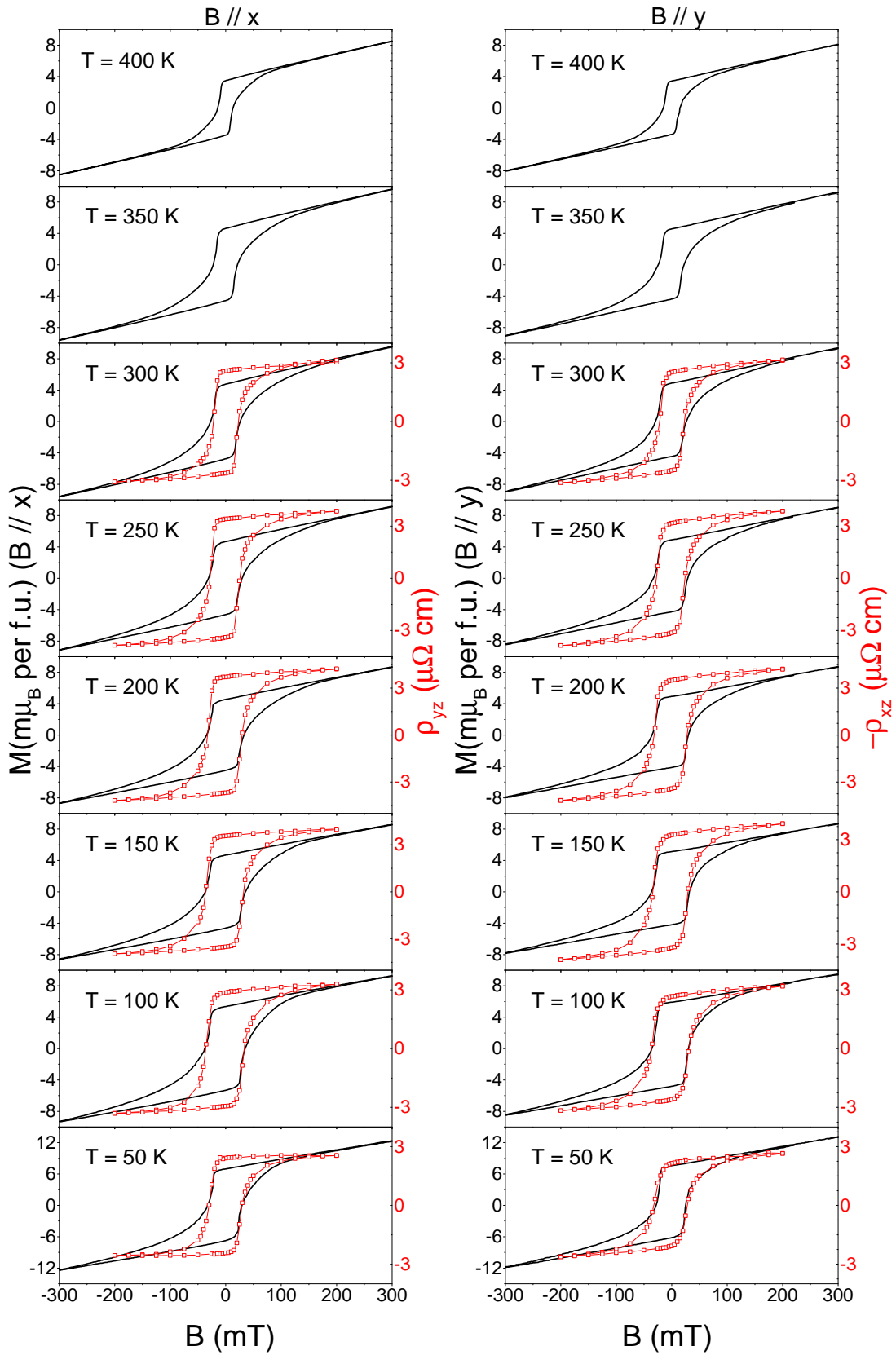


Figure 6: The magnetization and Hall resistivity as the magnetic field along x (left column) and along y (right column) at different temperatures.

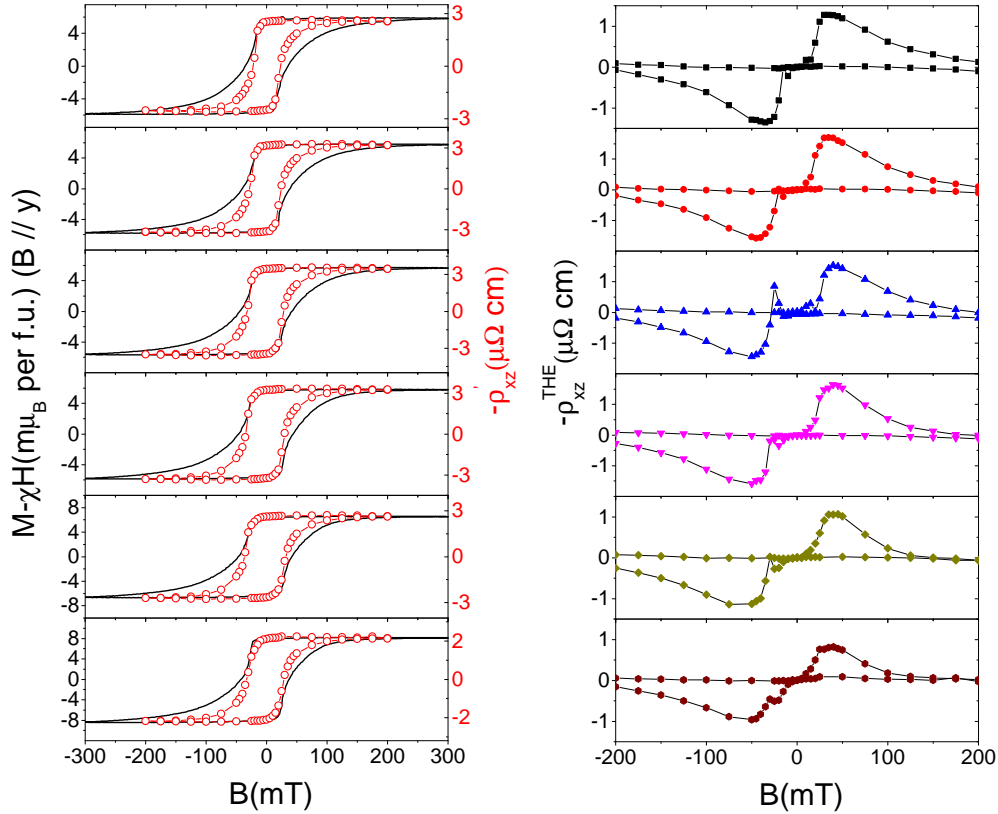


Figure 7: a) Comparison of the magnetization, with its high-field slope subtracted and anomalous Hall resistivity as the magnetic field is along the y axis. Similar to the case of a field along the x axis showed in the main text. The threshold field B_0 is identical, but the magnetization shows a slower variation at the end of the hysteresis loop. b) The topological Hall effect resolved by subtracting normalized magnetization times a constant from the Hall resistivity at different temperatures for a field along y axis.

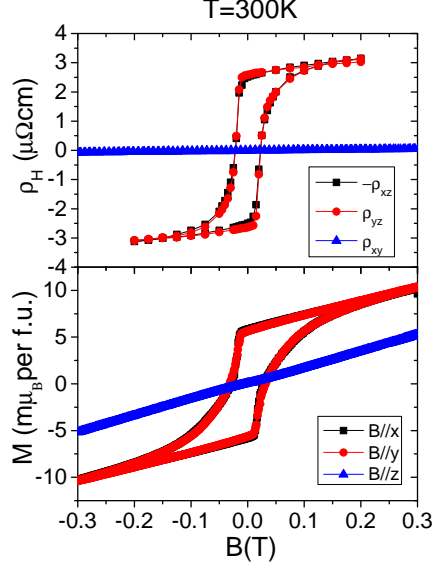


Figure 8: The magnetization and Hall resistivity for three high-symmetric axis at 300 K.

Samples	l_x	l_y	l_z	$-\rho_{xz}$	ρ_{yz}	$\rho_{xx,yy}$	ρ_{zz}	σ_{xz}	$-\sigma_{yz}$	$-\frac{\sigma_{xz}}{\sigma_{yz}}$
	mm	mm	mm	$\mu\Omega cm$	$\mu\Omega cm$	$\mu\Omega cm$	$\mu\Omega cm$	S/cm	S/cm	
#5	0.5	0.6	2	2.5	2.62		232.5	46.5	48.7	0.955
#6	0.42	0.38	1.7		2.99				53.7	
#10	2.05	2.5	1.75	3.05	2.92			54.8	52.5	1.044
#10-2	2.05	1.15	1.75	3.25	3.38			58.4	60.7	0.962
#10-8	0.5	0.2	1.75				240.6			
#12	0.22	1.31	0.53			229.0				
#14	0.6	2.5	0.14			231.2				
Average				2.93	2.98	230.1	236.55	53.23	53.9	0.987

Table 1: Anisotropy of anomalous Hall effect in different samples at 300 K.

E Anomalous Hall effect on different samples

We have measured several samples to check the repeatability of our results, which are summarized in table 1 for 300 K and 2 for 50 K. Restrictions caused by samples dimensions are the reason some measurements were not performed. As seen in the table, the magnitude of $\sigma_{yz}^A(B||x)$ and $\sigma_{xz}^A(B||y)$ were very close. Fig. S10 shows the temperature dependence of resistivity and anomalous Hall resistivity in various samples. Fig. S11 displays the temperature of anomalous Hall conductivity data for fields along the x and y axes compared to previous reports [?, 3].

F The extraction of B_s

We fitted the data between 0 to -200 mT for a positive to negative fields and 0 to 200 mT for negative to positive fields with an equation $\rho_{ij} = \rho_0(1 - 0.5e^{-B_s/B})$ to extract B_s^+ and B_s^- respectively. B_s is the average of B_s^+ and B_s^- . The fig. S12 shows the procedure of the

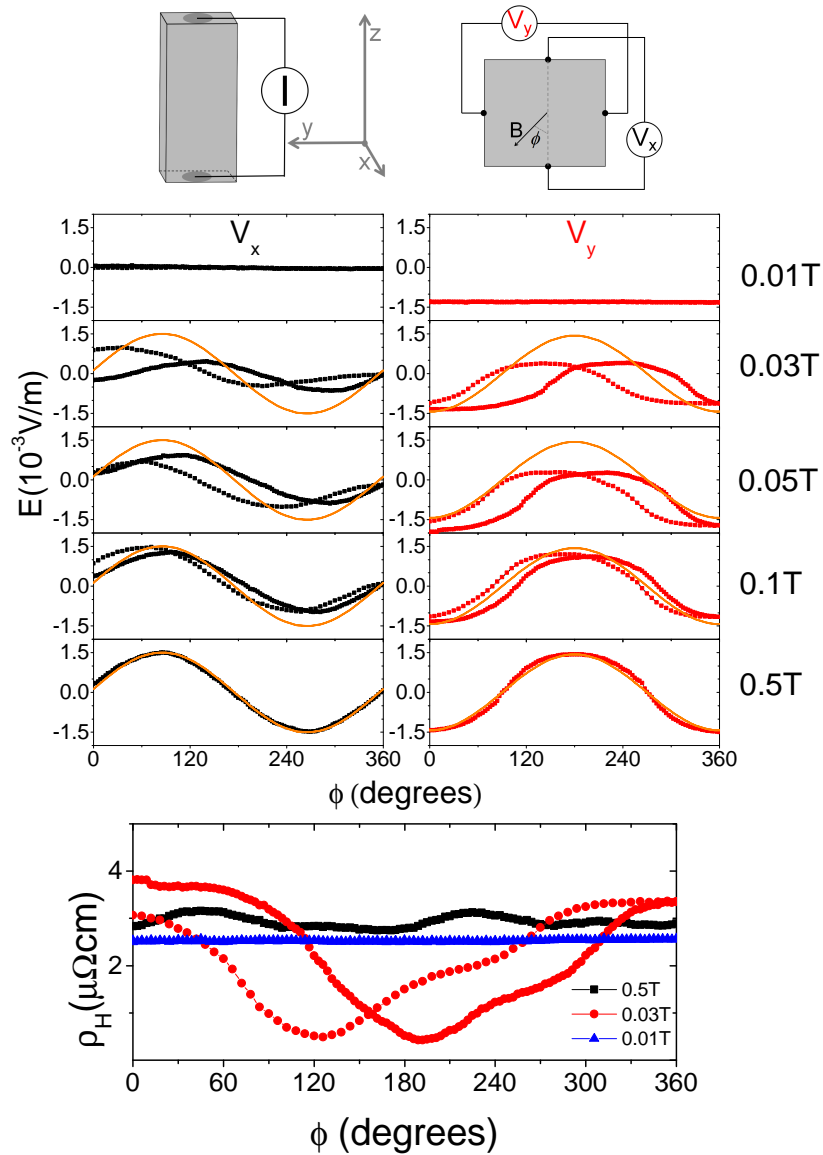


Figure 9: a) and b) Set-up for measuring angle-dependent Hall resistivity in a sample with a quadrate cross-section. The current was applied along the z axis and the magnetic field was rotated in the basal plane. Two pairs of electrodes monitored the electric field along the x and y axes. c) Angular variation of the E_x and d) the E_y as a function of the angle between the magnetic field and the x axis. At low magnetic field (regime I), the total electric field remains unchanged. At high magnetic field (regime III), for both orientations, the measured electric field presents almost sinusoidal variation with almost no hysteresis. In the intermediate field range (regime II), the angular variation is strongly hysteretic. (e) The total Hall resistivity as a function the angle.

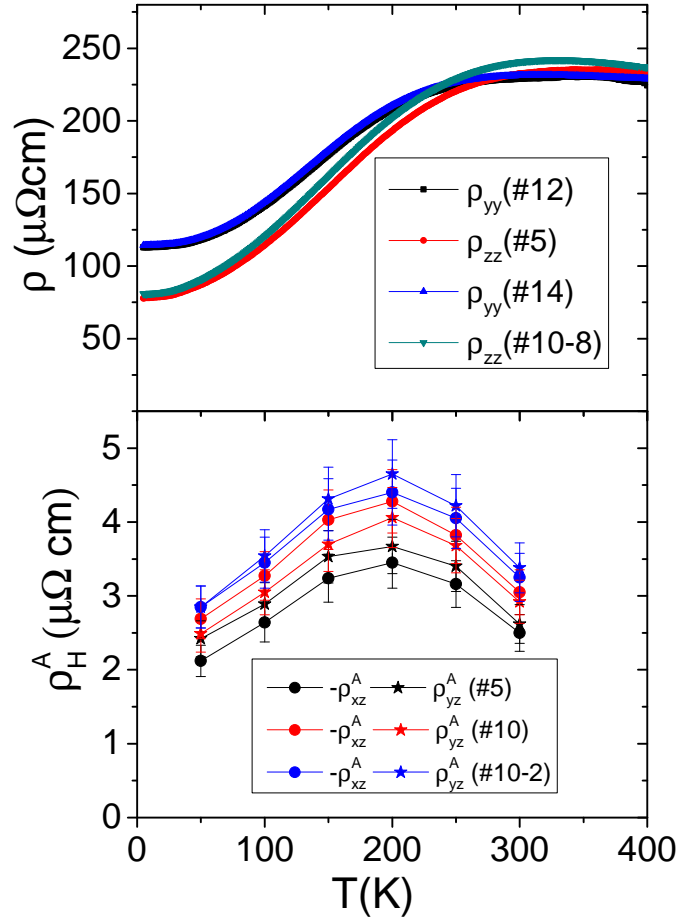


Figure 10: a) Temperature dependence of the ρ_{yy} and ρ_{zz} in various samples. Both ρ_{yy} and ρ_{zz} measured in two different samples respectively shows almost identical behavior. b). The anomalous Hall resistivity on various samples at several temperatures. Combining the data in a), we deduced the Hall conductivity of Fig.2 in the main text.

Samples	l_x	l_y	l_z	$-\rho_{xz}$	ρ_{yz}	$\rho_{xx,yy}$	ρ_{zz}	σ_{xz}	$-\sigma_{yz}$	$-\frac{\sigma_{xz}}{\sigma_{yz}}$
	mm	mm	mm	$\mu\Omega cm$	$\mu\Omega cm$	$\mu\Omega cm$	$\mu\Omega cm$	S/cm	S/cm	
#5	0.5	0.6	2	2.12	2.42		87.1	203.2	231.9	0.876
#6	0.42	0.38	1.7		2.95				271.0	
#10	2.05	2.5	1.75	2.69	2.49			247.1	228.8	1.08
#10-2	2.05	1.15	1.75	2.85	2.85			261.8	261.8	1
#10-8	0.5	0.2	1.75				90.8			
#12	0.22	1.31	0.53			118.2				
#14	0.6	2.5	0.14			119.8				
Average				2.55	2.68	119	88.95	237.4	248.4	0.985

Table 2: Anisotropy of anomalous Hall effect in different samples at 50 K.

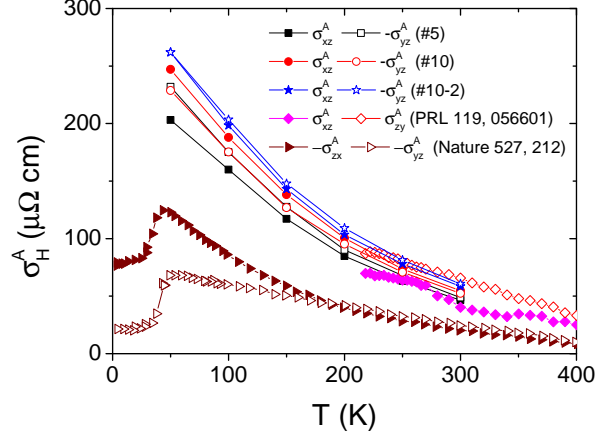


Figure 11: a) The temperature-dependence of anomalous Hall conductivity in different samples and in previous reports.

	σ_H^A	σ_H^{THE}	M	S_H	$\frac{\sigma_H^{THE}}{\sigma_H^A}$
	S/cm	S/cm	A/cm	V^{-1}	
MnSi	56 [15]	1.8 [15]	293.8 [16]	0.19	0.032
Mn ₃ Sn	232	113.7	10.75	21.6	0.49

Table 3: Comparison of magnetization and AHE in Mn₃Sn (at 50K) with MnSi (at 28 K).

extraction of B_s in sample # 13-2 at 300 K. B_s for other samples were obtained by repeating this procedure.

G Comparison with MnSi

The prototype spiral helimagnet MnSi has a non-trivial magnetic texture: a skyrmion lattice in its so-called A phase. Table 3 compares the physical properties of Mn₃Sn and MnSi. S_H^A is defined as σ_H^A/M . For MnSi, a large AHE emerges below its Curie temperature and is almost proportional to its magnetization across a wide temperature window. The amplitude of the AHE of Mn₃Sn is comparable to it at room temperature and 3 times larger at 100 K. While the magnetization of MnSi is 50 times larger than that of Mn₃Sn. So the S_H^A are two to three orders higher than that in MnSi. The magnitude of S_H (the ratio of AHC to magnetization [16]) is exceptionally large in the former as highlighted previously [3]. Remarkably, a large fraction of the AHC in Mn₃Sn is caused by real-space Berry curvature. As seen in the table, this is in sharp contrast with MnSi.

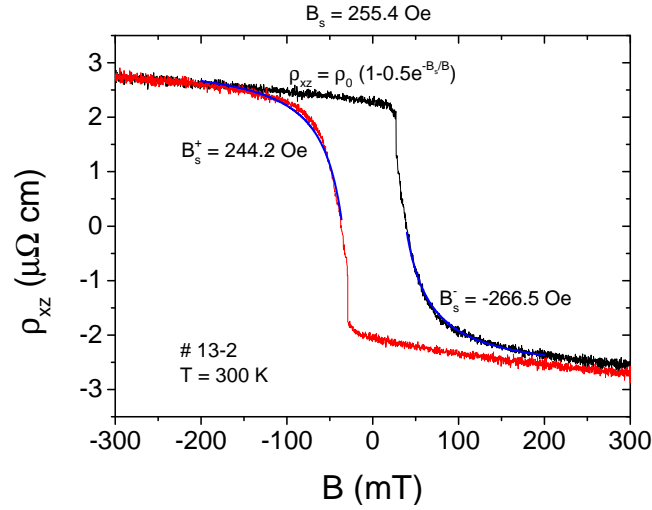


Figure 12: An example of extraction of B_s in the sample # 13-2 at 300 K

H Theoretical in-plane anisotropy

The calculated total energy of Mn_3Sn as a function of the uniform spin angle rotation is shown in Fig. S13, which gives an indication about the in-plane single-ion anisotropy. One can see that the variation with angle is less than the convergence criteria 0.045 meV/Mn used in the calculations. This result is in agreement with the experimental finding according to which the spins can rotate very easily with rotating magnetic field. The band structure was also calculated for three different spin orientations (Fig. S14). No visible difference can be seen.

`\bibliographystyle{SciPost_bibstyle}`

References

- [1] Zimmer, G. J. & Krén, E. Investigation of the Magnetic Phase Transformation in Mn_3Sn . AIP Conf. Proceed. **5**, 513 (1972)
- [2] Tomiyoshi, S., and Yamaguchi, Y. Magnetic Structure & Weak Ferromagnetism of Mn_3Sn Studied by Polarized Neutron Diffraction. J. Phys. Soc. Jpn. **51**, 2478 (1982).
- [3] Nakatsuji, S., Kiyohara, N., & Higo, T. Large anomalous Hall effect in a non-collinear antiferromagnet at room temperature. Nature **527**, 212 (2015).
- [4] Nayak, A. K. *et al.* Large anomalous Hall effect driven by a nonvanishing Berry curvature in the noncolinear antiferromagnet Mn_3Ge . Sci. Adv. **2**: e1501870 (2016).
- [5] Kiyohara, N., Tomita, T., & Nakatsuji, S. Giant anomalous Hall effect in the chiral antiferromagnet Mn_3Ge . Phys. Rev. Appl. **5**, 064009 (2016).

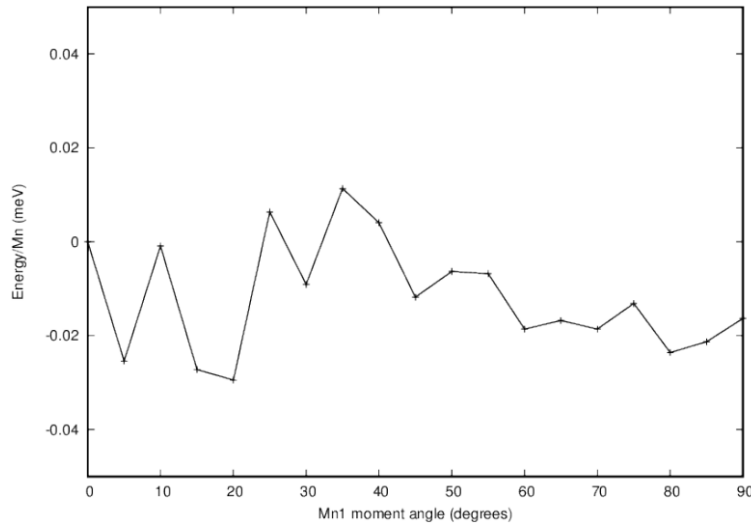


Figure 13: The angle dependence of single-ion anisotropy

- [6] Chen, H., Niu, Q., & MacDonald, A. Anomalous Hall effect arising from noncollinear antiferromagnetism. *Phys. Rev. Lett.* **112**, 017205 (2014).
- [7] Kübler, J. & Felser, C. Non-collinear antiferromagnets and the anomalous Hall effect. *Europhys. Lett.* **108**, 67001 (2014).
- [8] Ikhlas, M. *et al.* Large anomalous Nernst effect at room temperature in a chiral antiferromagnet. *Nat. Phys.* **13**, 1085 (2017)
- [9] Li, X., Xu, L., Ding, L., Wang, J., Shen, M., Lu, X., Zhu, Z. & Behnia, K. Anomalous Nernst and Righi-Leduc effects in Mn_3Sn : Berry curvature and entropy flow. *Phys. Rev. Lett.* **119**, 056601 (2017).
- [10] Haldane, F. D. M. Berry Curvature on the Fermi Surface: Anomalous Hall Effect as a Topological Fermi-Liquid Property. *Phys. Rev. Lett.* **93**, 206602 (2004).
- [11] Zhang Y. *et al.* Strong anisotropic anomalous Hall effect and spin Hall effect in the chiral antiferromagnetic compounds Mn_3X (X=Ge, Sn, Ga, Ir, Rh, and Pt). *Phys. Rev. B* **95**, 075128 (2017).
- [12] Dheer, P. N. Galvanomagnetic Effects in Iron Whiskers. *Phys. Rev.* **156**, 637 (1967).
- [13] Watzman, S. J. *et al.* Magnon-drag thermopower and Nernst coefficient in Fe, Co, and Ni. *Phys. Rev. B* **94**, 144407 (2016).
- [14] Kötzler, J. & Gil, W. Anomalous Hall resistivity of cobalt films: Evidence for the intrinsic spin-orbit effect. *Phys. Rev. B* **72**, 060412(R) (2005).
- [15] Neubauer, A., Pfeleiderer, C., Binz, B., Rosch, A., Ritz, R., Niklowitz, P. G., & Böni, P. Topological Hall Effect in the A Phase of MnSi . *Phys. Rev. Lett.* **102**, 186602 (2009).

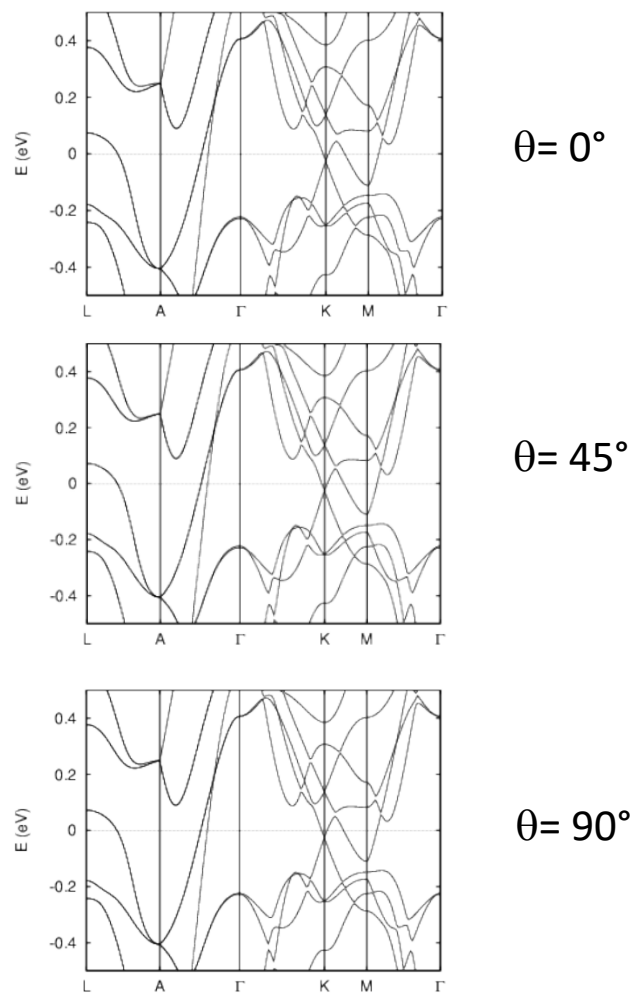


Figure 14: Band structure for three different spin orientations.

- [16] Lee, M., Onose, Y., Tokura, Y. & Ong, N. P. Hidden constant in the anomalous Hall effect of high-purity magnet MnSi. *Phys. Rev. B* **75**, 172403 (2007).
- [17] Jiles, D. C. & Atherton, D. L. Theory of ferromagnetic hysteresis. *J. Magn. Magn. Mater.* **61**, 48 (1986).
- [18] Chang, C. Z. *et al.* Experimental Observation of the Quantum Anomalous Hall Effect in a Magnetic Topological Insulator. *Science* **340**, 167 (2013).
- [19] Checkelsky, J. G., *et al.* Trajectory of the anomalous Hall effect towards the quantized state in a ferromagnetic topological insulator. *Nature Physics* **10**, 731 (2014).
- [20] Everschor-Sitte, K. & Sitte, M. Real-space Berry phases: Skyrmion soccer. *J. Appl. Phys.* **115**, 172602 (2014).
- [21] Mertelj, A., Lisjak, D., Drofenik, M. & Čopič, M. Ferromagnetism in suspensions of magnetic platelets in liquid crystal. *Nature* **504**, 237 (2013).
- [22] Liu, J. & Balent L. Anomalous Hall Effect and Topological Defects in Antiferromagnetic Weyl Semimetals: Mn₃Sn/Ge. *Phys. Rev. Lett.* **119**, 087202 (2017).
- [23] Zhang, D., Yan, B., Wu, S.-C., Kübler, J., Kreiner, G., Parkin, S. S. P., & Felser, C. First-principles study of the structural stability of cubic, tetragonal and hexagonal phases in Mn(3)Z (Z=Ga, Sn and Ge) Heusler compounds, *J. Phys.: Condens. Matter* **25** 206006 (2013).
- [24] Suzuki, M.-T., Koretsune, T., Ochi, M. & Arita, R.. Cluster multipole theory for anomalous Hall effect in antiferromagnets. *Phys. Rev. B* **95**, 094406 (2017)
- [25] Yang, H. *et al.* Topological Weyl semimetals in the chiral antiferromagnetic materials Mn₃Ge and Mn₃Sn. *New J. Phys.* **19** 015008(2017).
- [26] Kübler, J. & Felser, C. Weyl Fermions in antiferromagnetic Mn₃Sn and Mn₃Ge. [arXiv:1711.03891](https://arxiv.org/abs/1711.03891) (2017).
- [27] Kuroda, K., et al., Evidence for magnetic Weyl fermions in a correlated metal. *Nat. Mater.* **16**, 1090 (2017).
- [28] Nagaosa, N., Yu, X. Z., & Tokura, Y.. Gauge fields in real and momentum spaces in magnets: monopoles and skyrmions. *Philos. Trans. R. Soc., A* **370**, 5806 (2012).
- [29] Freimuth, F., Bamler, R., Mokrousov, Y., & Rosch, A.. Phase-space Berry phases in chiral magnets: Dzyaloshinskii-Moriya interaction and the charge of skyrmions. *Phys. Rev. B* **88**, 214409 (2013).
- [30] Liu, C., Zang, Y., Ruan, W., Gong, Y., He, K., Ma, X., Xue, Q.-K., & Wang, Y. Dimensional Crossover-Induced Topological Hall Effect in a Magnetic Topological Insulator. *Phys. Rev. Lett.* **119**, 176809 (2017).
- [31] Soumyanarayanan, A. *et al.* Tunable room-temperature magnetic skyrmions in Ir/Fe/Co/Pt multilayers. *Nature Materials* **16**, 898 (2017).

- [32] Bruno, P., Dugaev, V. K., & Taillefumier, M.. Topological Hall Effect and Berry Phase in Magnetic Nanostructures. *Phys. Rev. Lett.* **93**, 096806 (2004).
- [33] Nagaosa, N. & Tokura, Y., Topological properties and dynamics of magnetic skyrmions. *Nat. Nano.***8**, 899 (2013)
- [34] Tomoya, H. *et al.*, Large magneto-optical Kerr effect and imaging of magnetic octupole domains in an antiferromagnetic metal. *Nature Photonics* **12**, 73 (2018).
- [35] Tetienne J.-P. *et al.* , The nature of domain walls in ultrathin ferromagnets revealed by scanning nanomagnetometry, *Nature Communications* **6** :6733 (2015).
- [36] Perdew J. P., Burke K., & Ernzerhof J. P. , Generalized Gradient Approximation Made Simple, *Phys. Rev. Lett.* **77**, 3865 (1996).
- [37] <http://elk.sourceforge.net>
- [38] Tomiyoshi S., Polarized Neutron Diffraction Study of the Spin Structure of Mn₃Sn *J. Phys. Soc. Jpn.* **51**, 803 (1982).
- [39] Brown P., Nunez V., Tasset F., Forsyth J., and & Radhakrishna P., Determination of the magnetic structure of Mn₃Sn using generalized neutron polarization analysis, *J. Phys. Condens. Matter* **2**, 9409 (1990).